AIAA JOURNAL
Vol. 30, No. 8, August 1992

Joint Computational/Experimental Aerodynamics Research on a Hypersonic Vehicle, Part 2: Computational Results

Mary McWherter Walker* and William L. Oberkampf†
Sandia National Laboratories, Albuquerque, New Mexico 87185

Parabolized and iterative Navier-Stokes codes are used to predict flowfield solutions around a hypersonic vehicle. Aerodynamic force and moment predictions from the codes are compared with experimental data from the Sandia National Laboratories Mach 8 wind tunnel. The comparisons are made on a spherically blunted cone with a slice parallel to the body axis. On the slice portion of the vehicle, a flap can be attached so that deflection angles of 10, 20, and 30 deg can be obtained. The Sandia parabolized Navier-Stokes code is used to generate solutions for the sliced vehicle with no flap. For the vehicle with a flap, axially separated flow occurs, and a time iterative Navier-Stokes code is used to provide comparisons with the data. Aerodynamic force and moment comparisons are made for laminar flow, and an ideal gas is assumed in the calculations. A detailed study of grid convergence is presented to determine the accuracy of the numerical solutions. Predictions obtained from the codes show very good agreement with the experimental data for force and moment coefficients, except for large flap deflections.

Nomenclature

C_a = forebody axial force coefficient, $A/(q_\infty S)$
C_m = pitch moment coefficient, $M/(q_\infty S D_b)$, referenced about $x/L = 0.5$
C_n = normal force coefficient, $N/(q_\infty S)$
D_b = diameter of the base
L = body length, 10.391 in.
M_∞ = freestream Mach number
q_∞ = freestream dynamic pressure
R_L = freestream Reynolds number based on body length
r_b = radius of the base, 2.0 in.
r_n = radius of the nose, 0.2 in.
S = reference area, 11.525 in.^{2}
T_o = total temperature
T_w = model wall temperature
T_∞ = freestream temperature
x_{cp} = axial center of pressure measured from the nose
α = angle of attack, positive when slice on windward side
δ = flap deflection angle
ζ = transformed body axis normal coordinate
η = transformed circumferential coordinate
ξ = transformed streamwise coordinate
ϕ = model roll angle, 0 deg for slice on windward side at positive α

Introduction

THE realization that certain flowfields can be computed more accurately than they can be measured experimentally should begin to change the relationship between computational and experimental aerodynamics. This paper and its companion[1] address this changing relationship and seek to improve the synergism between computational aerodynamics and wind-tunnel experimentation. The purpose of this project is to improve the confidence and accuracy in both computational aerodynamic predictions and wind-tunnel measurements. The numerical and physical approaches can each gain from this joint endeavor by using the strengths of one approach to offset the weaknesses of the other, and vice versa. In this project, computations and experiments were conducted for perfect gas, laminar flow over a hypersonic vehicle geometry. The model geometry was designed so that it could be modified easily to produce a range of flow characteristics. For the simplest configuration, we developed higher confidence in the accuracy of the computational fluid dynamics (CFD) solutions than the experiment. For the more complex configurations, however, the reverse was true.

In this paper, computational results are obtained for a 10-deg half-angle spherically blunted cone with a slice parallel to the cone axis. Aerodynamic force and moment predictions are compared with wind-tunnel data from the Sandia Mach 8 hypersonic wind tunnel. These comparisons are made on a sliced vehicle both with and without a windward flap. The dimensions of the vehicle are shown in Fig. 1. The windward flap can be deflected 10, 20, or 30 deg. The Sandia parabolized Navier-Stokes (PNS) code is used to generate solutions for the sliced vehicle. For the geometry with the flap deflected, reversed flow occurs, and a time iterative Navier-Stokes code is used to provide comparisons with the data. Force and moment and surface flow visualization comparisons are made for laminar, ideal gas flow. More complete experimental results for the same geometry and wind-tunnel conditions are given in Ref. 1.

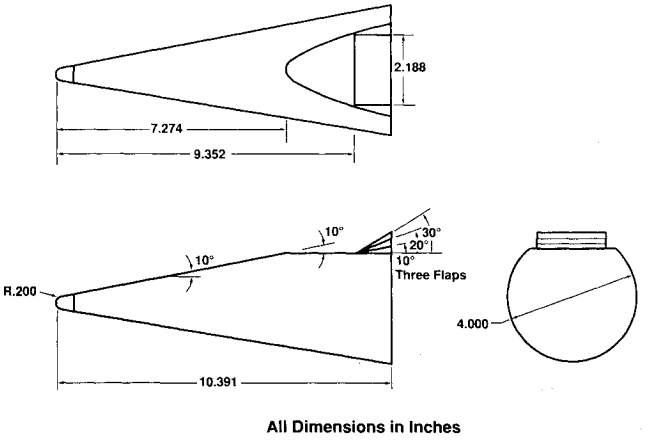

Fig. 1 Wind-tunnel model.

Presented as Paper 91-0321 at the AIAA 29th Aerospace Sciences Meeting, Reno, NV, Jan. 7-10, 1991; received March 9, 1991; revision received Jan. 30, 1992; accepted for publication Jan. 30, 1992.

*Senior Member Technical Staff, Computational Fluid Dynamics Department. Senior Member AIAA.
†Senior Member Technical Staff, Aerodynamics Department. Associate Fellow AIAA.

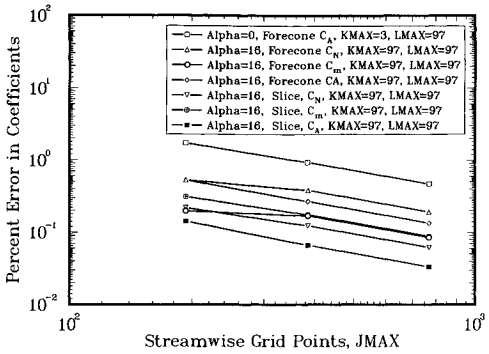

Fig. 2 Error in force and moment coefficients vs *JMAX*.

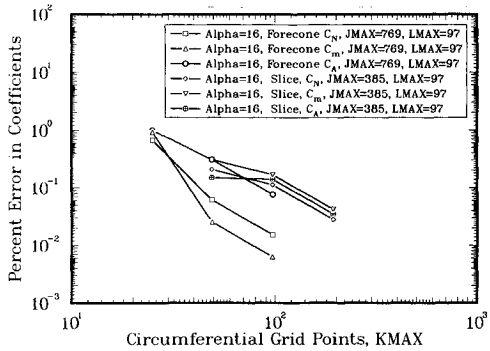

Fig. 3 Error in force and moment coefficients vs *KMAX*.

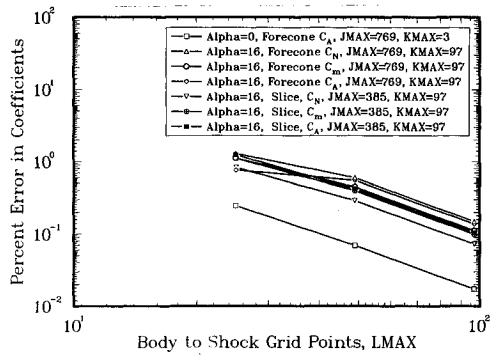

Fig. 4 Error in force and moment coefficients vs *LMAX*.

Computational Aerodynamics Codes

Two types of numerical approaches were used for comparison with, and evaluation of, the experimental measurements: a PNS approach and a time iterative Navier-Stokes approach. The PNS approach is able to tightly couple the viscous and inviscid flows and accurately simulate crossflow separation. The PNS approach can be used for all supersonic flows as long as the axial flow remains in the streamwise direction. Time iterative Navier-Stokes solutions were computed only in regions where the flow is subsonic or axially separated. A summary of the two solution techniques follows.

Blunt Nose Solution for Parabolized Navier-Stokes Calculations

To obtain PNS solutions over a blunt-nosed vehicle, the three-dimensional, subsonic and supersonic flow over the spherical nose is calculated first by using the thin-layer, time-iterative, Navier-Stokes equations. The three-dimensional Navier-Stokes (NS3D) code[2,3] is used to compute the flowfield around the nose. The NS3D code provides a starting solution for the PNS code, which is used to advance the flowfield solution along the body. The NS3D equations are obtained from the unsteady Navier-Stokes equations by neglecting the viscous derivatives in the streamwise and circumferential directions. The viscous derivatives are retained only in the normal direction. This is referred to as the thin-layer model. The same viscous terms that are dropped in boundary-layer theory are also dropped in the thin-layer model. However, the vertical momentum equation is retained, and a constant pressure is not imposed through the viscous layer. Unlike boundary-layer theory, the thin-layer model avoids the difficulty of matching an inviscid layer with a viscous layer.

NS3D solves the continuity, momentum, and energy equations in a body-fitted, shock-fitted transformed space. The equations are solved by approximating all partial derivatives by finite difference expressions. The difference equations are solved by an unsteady, implicit algorithm. Block tridiagonal systems are inverted in each space coordinate at each time step. The solution is advanced in time until a steady-state, i.e., converged, solution is reached.

Parabolized Navier-Stokes Solution

The PNS equations are thin-layer Navier-Stokes equations with an approximation for the convective flux vector. These assumptions permit stable timelike marching of the equations downstream from initial data. The latter assumption does not permit calculation of flows that have separation in the axial direction. Three-dimensional crossflow separation, however, is permitted. The stated approximations are physically justified for high to moderate Reynolds number flow past bodies with mild axial geometry changes.

The PNS equations are also solved in a body-fitted, shock-fitted transformed space. The finite difference form of the PNS equations are formulated into an approximately factored, locally linearized form. The numerical solution is a noniterative, implicit, finite-difference algorithm. The difference equations are treated in vector form, and their solution requires a factored sequence of block-tridiagonal equations. The equations are solved by inverting the block-tridiagonal systems in the two crossflow plane coordinates at each location of the marching coordinate. The flow is solved by marching the finite difference equations in planes normal to the axis of the vehicle. Two initial planes of supersonic flow data to start the PNS code are provided by the NS3D code. The afterbody portion is then solved by marching the PNS equations along the body up to the base of the vehicle.

The Sandia Parabolized Improved Navier-Stokes Technique (SPRINT) code,[4] currently in use at Sandia, is an extensively modified version of the Air Force Wright Aeronautical Laboratory (AFWAL) parabolized Navier-Stokes code.[5] It is based on the work of Schiff and Steger[6] and others.[7-9] Many significant changes were made to the AFWAL code, some of which are documented in Ref. 4. Sandia has spent several years developing and verifying the SPRINT code by comparing it with experimental data. The code has predicted forces and

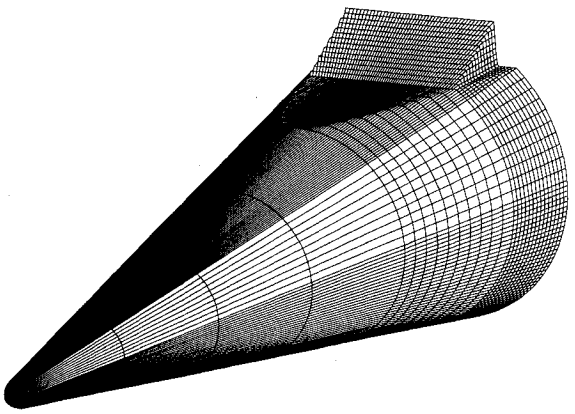

Fig. 5 Surface grid for 30-deg flap deflection, *KMAX* = 91 in half-plane.

moments, surface pressure, and heat transfer for different re-entry vehicles and flow conditions.[10-13]

Continuation Navier-Stokes Solution

It was anticipated that the sliced vehicle with a large flap deflection would generate a reversed flow region upstream of the flap. To calculate the flow in this region, the SPRINT code was marched to a point ahead of the reversed flow region, and a time iterative Navier-Stokes solution was used to provide the solution over the separated region. The separated region was solved using the F3D code, which was developed by Steger and others.[14-16] It solves the same set of thin-layer Navier-Stokes equations described for NS3D, but using a different numerical scheme. The F3D code uses an implicit approximately factored scheme that uses central differences in the circumferential η and normal ζ directions and upwinding in the streamwise ξ direction. The streamwise flux vector has been eigensplit, allowing the use of backward and forward difference operators.

The F3D code was used to obtain the flowfield solutions for the 10-, 20-, and 30-deg flap deflections. The F3D code was used in the continuation mode with an ideal gas assumed. The flowfield grid was provided using the parabolic grid generator in the SPRINT code. The SPRINT solution just ahead of the start of the vehicle slice was imposed over the entire flowfield grid to be used as a starting condition for F3D. The F3D code was then iterated in time until a steady-state solution was reached. Convergence was assumed when the normalized residuals reached values of 10^{-6} or less.

Evaluation of Accuracy of Numerical Simulation

Richardson Extrapolation

To verify quantitatively the accuracy of the computational results, a detailed grid refinement study was performed. Since the force and moment coefficients were compared with experimental data, they were used as the representative parameters in the study. In addition, smoothing and stabilizing parameters were kept to a minimum (zero in some cases) during the grid refinement studies.

The grid refinement study presented in this paper is an extension of the work presented by Blottner.[17] The grid is refined in each direction of the three dimensions while holding the other two dimensions fixed. The Richardson extrapolation[18] is used to obtain an estimated "exact" solution as the number of grid points approaches infinity. When the parameter of interest, for example, axial force coefficient, is less than 1% in error from the estimated exact solution, the grid is considered to be adequately refined for accurate predictions of the given parameter. For a one-dimensional problem solved with an nth-order numerical scheme, the exact solution Q_E can be expressed in terms of the numerical solution Q_N and the truncation errors as follows:

$$Q_E = Q_N + \alpha\Delta^n + \text{higher-order terms} \tag{1}$$

The coefficient α is to be determined from the numerical solutions. Numerical results are obtained with grid step size Δ and 2Δ. With the higher-order terms neglected in the expression, two different grid solutions are combined to eliminate α and obtain

$$Q_E = Q_N(\Delta) + \frac{1}{2^n - 1}\left[Q_N(\Delta) - Q_N(2\Delta)\right] \tag{2}$$

The numerical solutions are obtained on a series of grids where, on each refinement, the number of grid points is doubled and the mesh spacing is halved. The number of grid points in each grid is related to the basic grid ($J_0 \times K_0 \times L_0$) by the relations $J_m - 1 = 2^m (J_0 - 1)$, $K_m - 1 = 2^m (K_0 - 1)$, and $L_m - 1 = 2^m (L_0 - 1)$, where $m = 1,2,3,\ldots$. The exact solution estimate when the grid is refined in the ξ-coordinate direction, which is first order in the SPRINT code, becomes

$$Q_E(J \to \infty) = Q_{N_m} + (Q_{N_m} - Q_{N_{m-1}}) \tag{3}$$

holding K_m and L_m constant and neglecting higher-order terms. Because the SPRINT code is second order in the η and ζ directions, the exact solution estimates for the other two directions can be expressed as

$$Q_E(K \to \infty) = Q_{N_m} + \tfrac{1}{3}(Q_{N_m} - Q_{N_{m-1}}) \tag{4}$$

$$Q_E(L \to \infty) = Q_{N_m} + \tfrac{1}{3}(Q_{N_m} - Q_{N_{m-1}}) \tag{5}$$

When the appropriate grid size is determined for each direction, the accuracy of the solution can be evaluated for all three dimensions simultaneously using the following equation:

$$Q_E = Q_N + \alpha\Delta_\xi^n + \beta\Delta_\eta^n + \gamma\Delta_\zeta^n + \text{higher-order terms} \tag{6}$$

For the SPRINT code, which is first-order accurate in the marching direction and second-order accurate in the circumferential and radial directions, the exact solution is estimated by

$$Q_E = Q_N + \alpha\Delta_\xi + \beta\Delta_\eta^2 + \gamma\Delta_\zeta^2 \tag{7}$$

Table 1 Grid convergence study

Case	*JMAX*, axial	*KMAX*, circumferential	*LMAX*, radial	Selected grid $J \times K \times L$
$\alpha = 0$ deg	769	3	97	
Forecone	385	3	49	$385 \times 3 \times 49$
	193	3	25	
$\alpha = 16$ deg	769	97	97	
Forecone	385	49	49	$385 \times 49 \times 49$
	193	25	25	
$\alpha = 16$ deg	769	193	97	
Sliced	385	97	49	$193 \times 49 \times 49$
portion	193	49	25	

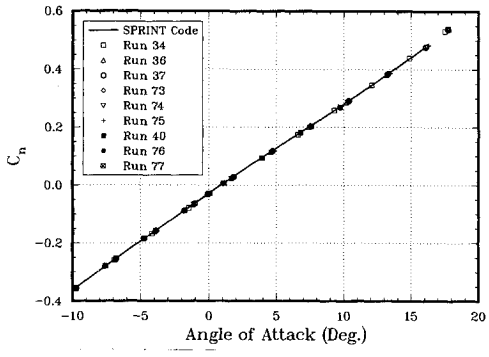

Fig. 6 Normal force coefficient for slice-only configuration.

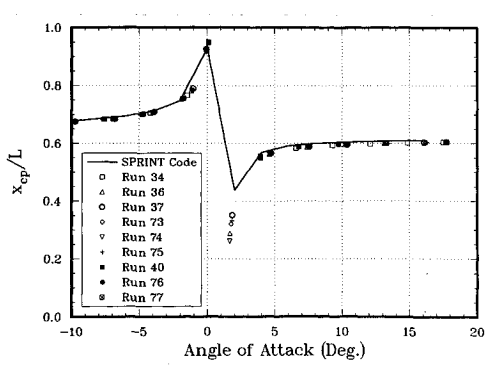

Fig. 7 Center of pressure for slice-only configuration.

Table 2 Freestream conditions

M_∞	7.84
R_L	1.80×10^6
T_o	1106°R
q_∞	1.727 psi
T_{wall}	570°R

The coefficients α, β, and γ are evaluated by obtaining numerical solutions with grid step sizes Δ and 2Δ for each direction while holding the other two directions fixed.

The grid study was performed for three cases. First, for the forecone of the sliced vehicle (forward of $x/L = 0.7$) at $\alpha = 0$ deg; second, for the forecone of the sliced vehicle at $\alpha = 16$ deg; and third, for the sliced portion of the vehicle (aft of $x/L = 0.7$) at $\alpha = 16$ deg. The forecone solutions were refined separately from the sliced portion of the vehicle. This was done because the two portions of the SPRINT solutions were obtained separately. The sliced portion of the vehicle solution was obtained by restarting the SPRINT code just ahead of the slice and respacing the flowfield grid to march on the slice.

Table 1 shows the selected values for *JMAX, KMAX,* and *LMAX* for the grid study. Solutions were obtained for all three values of *JMAX* while using fixed values of *KMAX* and *LMAX*. Solutions were obtained while varying *KMAX* and *LMAX* in a similar manner. As shown in Figs. 2–4, the fixed values were always twice the converged grid values shown in Table 1 for each case. The value for *KMAX* was held constant at 3 for the $\alpha = 0$ deg solutions because the solution is axisymmetric and the SPRINT code uses cylindrical coordinates. More detailed information on the error analysis of the computational results can be obtained in Ref. 19.

Grid Refinement Results

The percent errors for each case and force and moment coefficient are plotted in Figs. 2–4. The validity of the Richardson extrapolation for the grid sizes used is demonstrated by noting that the negative slope of the lines in the figures should be the same as the order of the solution. For the lines shown in Fig. 2, the slope should be -1. For the lines shown in Figs. 3 and 4, the slope should be -2. The points shown in Fig. 2 exhibit the expected behavior except for the normal force and pitch moment curves for the forecone at $\alpha = 16$ deg. It is felt that any nonlinearity is probably due to required values of smoothing and stabilizing parameters in the SPRINT solutions. Similar results are shown in Figs. 3 and 4 for the refinement in *KMAX* and *LMAX*. The accepted values for *JMAX, KMAX,* and *LMAX* for each portion of the body are shown in the last column of Table 1.

In addition to computing the exact solution in each direction as if it were a one-dimensional problem, the exact solution was computed using Eq. (7). The percent error from the three-dimensional exact solution was computed to determine if the selected grid parameters produced answers that fell within the accepted error. For all three cases, the solutions using the selected grid sizes shown in Table 1 fell within the 1% bound for the fully three-dimensional error estimate.

To anticipate the more complex flow when the flap was deflected, the number of circumferential grid points was arbitrarily increased from 49 to 91 (in the half-plane). Figure 5 shows the vehicle surface grid used for the $\delta = 30$ deg SPRINT/F3D solutions. It was felt that 91 circumferential grid points would adequately resolve the flow in the region of the flap, but as opposed to the previous quantitative error analysis, this was purely intuitive. Grid refinement studies were not performed using the F3D code due to the large computing costs. The number of axial points was thinned (SPRINT used 193) because of computer memory limitations. The number of points selected for the axial direction for F3D was 93 (from the start of the slice to the end of the flap). To capture the outer bow shock in F3D, 10 additional radial grid points were added, yielding 59.

Results

Comparisons of computational and experimental results are presented for force and moment coefficients, center of pressure, and surface flow visualization. Table 2 gives the freestream conditions and wall temperature boundary condition. A more complete description of the experiment and experimental data is given in Ref. 1. For all of the comparisons on the sliced vehicle, solutions were obtained using NS3D/SPRINT. For comparison of results on the vehicle with a 10-deg flap deflection, solutions were obtained using both the NS3D/SPRINT and NS3D/SPRINT/F3D codes. For the 10-, 20-, and 30-deg flap deflection cases, the SPRINT code was marched up the start of the slice, and the F3D code was used to obtain solutions over the region containing the slice and flap.

Slice-Only Configuration

The force and moment comparisons for the sliced vehicle are shown in Figs. 6–8. As shown in Fig. 6, the SPRINT code shows excellent agreement with the measurements for normal force coefficient. The slice was located on the windward side of the vehicle for positive angles of attack and on the leeward

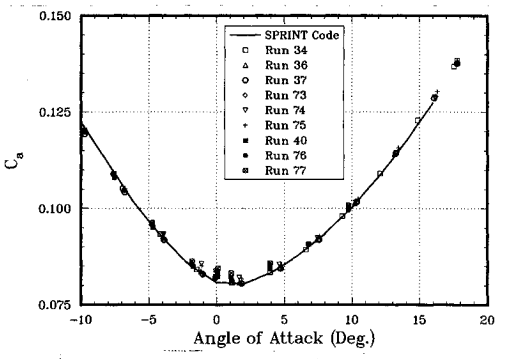

Fig. 8 Axial force coefficient for slice-only configuration.

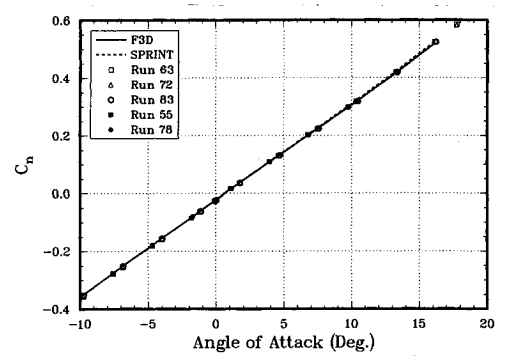

Fig. 9 Normal force coefficient for 10-deg flap deflection.

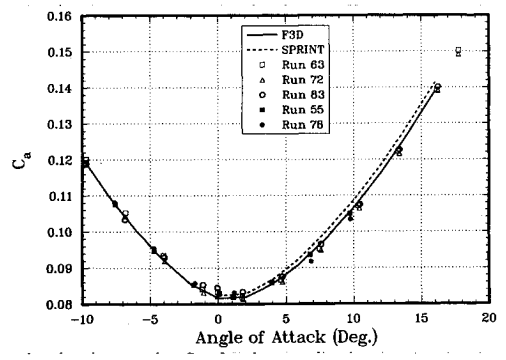

Fig. 10 Axial force coefficient for 10-deg flap deflection.

side of the vehicle for negative angles of attack. Data from all wind-tunnel runs of the same body geometry are plotted in the figures to evaluate the uncertainty of the wind-tunnel data (see Ref. 1 for details).

Figure 7 shows the computational and experimental results for the axial center of pressure. (All CFD results were computed in angle-of-attack increments of 2 deg. Linear interpolation, which can be misleading, was then used to construct the continuous curves shown in the figures.) Good agreement exists between computations and experiment, but there is a troublesome $0.01L$ difference in the results over the entire angle-of-attack range. Based on the quantitative error analysis discussed earlier, it is doubtful this is an error in the computational results. If the disagreement is due to nonuniformities in the test section flowfield, this could be verified, and eliminated, by inserting the actual measured flowfield from the wind-tunnel into the computations. Future plans for this joint computational/experimental program include finely spaced measurements of the Mach number, pressure, and flow angularity in the test section of the wind tunnel. The actual flowfield of the wind tunnel could then be used as nonuniform shock boundary conditions in the computational simulations.

Figure 8 shows the comparison between the computational and experimental data for the forebody ($p_{base} = p_\infty$) axial force coefficient. Very good agreement between the computations and experimental measurements is observed at large angles of attack, but near zero angle of attack, the experimental data are two counts higher than the computations. In an attempt to discover the cause of this discrepancy, it was noted that the low angle-of-attack data are measured during the early part of a wind-tunnel run. Early in the run, the model is cooler than the average wall temperature of 570°R used in the calculations. A separate calculation for $\alpha = 0$ was made with the wall temperature 30 deg cooler. This calculation showed only a 0.03 count decrease in axial force. Therefore, the discrepancy for small angle of attack remains unresolved. An improvement in base pressure measurement, as discussed in Ref. 1, may resolve this discrepancy.

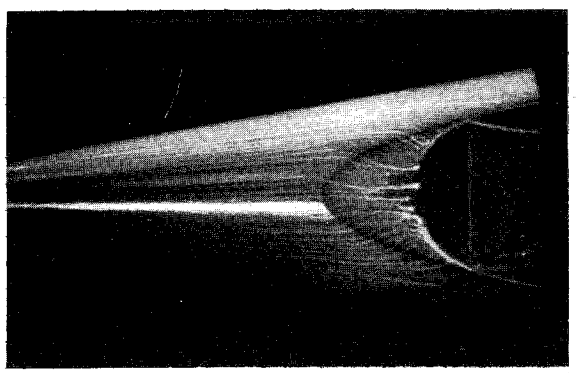

a) Experimental surface flow

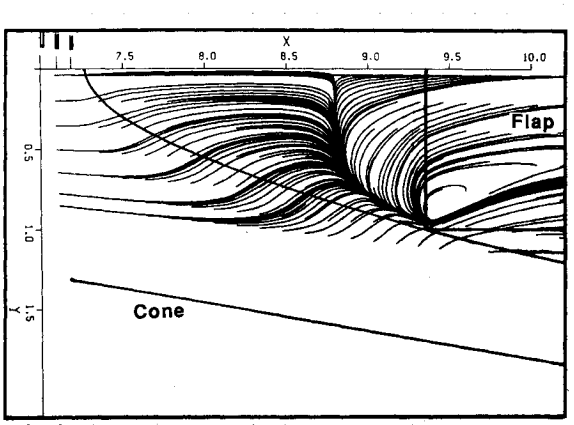

b) F3D surface particle trace.

Fig. 11 Surface flow for 10-deg flap deflection.

Flap Deflection Configuration

The sliced vehicle with a 10-deg flap deflection represents a geometry where the SPRINT solutions begin to come into question. For a 10-deg flap deflection, the laminar boundary layer may axially separate ahead of the flap, and there will certainly be crossflow separation in the corner formed by the side of the flap and the slice. For this reason, the F3D code was also used to obtain the flowfield solutions over the deflected flaps.

Figures 9 and 10 show the comparisons between the experiment and the NS3D/SPRINT and NS3D/SPRINT/F3D codes for the body with 10-deg flap deflection. In these figures, the NS3D/SPRINT combination is referred to as SPRINT, and the NS3D/SPRINT/F3D is referred to as F3D. Agreement between the SPRINT and F3D codes and the experimental data for normal force is quite good and similar to that for the vehicle with no flap. For the axial force coefficient, Fig. 10, the F3D code shows noticeably better agreement with the data than SPRINT. This is expected because of the reversed flow region ahead of the flap. The SPRINT code overpredicts the pressure on the flap, which results in a high prediction for axial force coefficient. The SPRINT solutions were harder to obtain with the flap deflection as compared to the sliced body and required additional numerical damping and stabilizing parameters. SPRINT obviously could not predict the axially separated flow in front of the flap, but it did predict an attached flow. Users of PNS codes are cautioned that a solution may be obtainable even though physically there is a thin reversed flow region.

Figure 11 shows a comparison of the experimental oil flow and particle trace lines predicted by the F3D code for zero angle of attack and a 10-deg flap deflection. The experimental surface flow visualization shows an axially separated flow region ahead of and onto the flap. Comparing the experimental oil flow and the computational traces (note the difference in scale), it is seen that the code accurately predicts the forward extent of the separated flow region, but the lateral (spanwise) extent is underpredicted. Also, the F3D code predicts a thin layer of negative axial velocities at the last axial solution plane. This implies that the flow never reattaches onto the flap and flow is moving onto the flap from the base of the vehicle. The F3D code does not solve the region on the base and, therefore, the solutions become questionable. The code uses an outflow boundary condition that dictates that the last plane of data be the same as the next to last plane. This is a first-order boundary condition that could be improved.

Figure 12 presents computational and experimental results for axial force coefficient for a flap deflection of $\delta = 20$ deg. The comparisons at positive angles of attack disagree by as much as 10%. The axial force comparisons are in good agreement for the negative angles of attack. This is only fortuitous, however, because the low pressure on the leeward side of the vehicle causes a loss in effectiveness of the flap. The F3D solutions have been carefully examined, and shortcomings in neither the numerical approximations nor the grid structure can be found. It is possible that the flow from the base needs to be coupled with the solution over the rest of the vehicle. If this is true, it could significantly increase the complexity and cost of CFD solutions that have large separated regions extending through outflow boundaries.

Figures 13 and 14 show results for the center of pressure and axial force coefficient for the 30-deg flap deflection. It is seen from Fig. 13 that the computational results for the center of pressure are in error up to $0.07L$ for positive angles of attack. The F3D code also disagrees with the axial force coefficient measurements, Fig. 14, as much as 20% at positive angles of attack. The F3D surface grid definition used 91 points in the circumferential half-plane, but this may not be sufficient to accurately compute the three-dimensional flow off the sides of

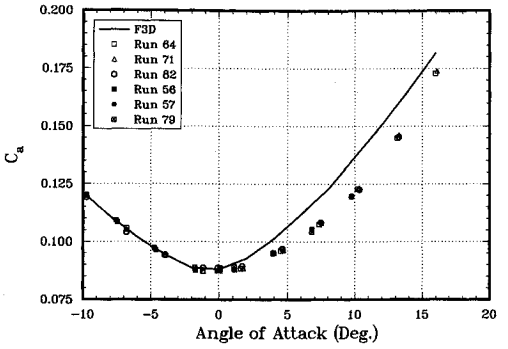

Fig. 12 Axial force coefficient for 20-deg flap deflection.

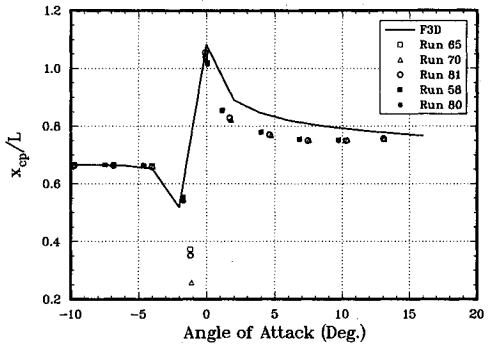

Fig. 13 Center of pressure for 30-deg flap deflection.

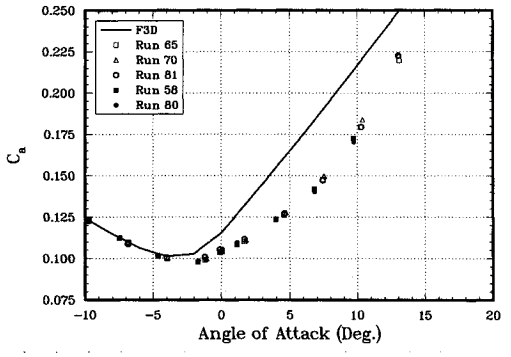

Fig. 14 Axial force coefficient for 30-deg flap deflection.

the slice and flap. The spanwise pressure variation was inspected in the region of the flap, and it appears to be reasonable for this type of flow. The magnitude of the pressure is seriously questioned, however, because the computational results for axial force are much larger than the experiment. (Reference 1 gives surface flow photographs for flap deflections of 10, 20, and 30 deg.) Another factor that may enter into the disagreement between computations and experiment is that reattachment of the free-shear layer onto the flap is probably turbulent. Transition and turbulent flow are not in the present numerical simulation.

In an attempt to identify the computational shortcomings, two additional computations were made. First, the F3D solution at $\alpha = 8$ deg and $\delta = 30$ deg was allowed to converge an additional 800 time steps, but this had no effect on center of pressure or axial force coefficient prediction. An additional calculation was made with 151 grid points circumferentially in the half-plane for $\alpha = 8$ deg and $\delta = 30$ deg, but this did not significantly affect the axial force. The 20- and 30-deg flap deflection cases present complex, massively separated flows that other researchers should attempt to compute.

Conclusions

Parabolized and iterative Navier-Stokes codes were used to predict flowfield solutions around a hypersonic vehicle with a slice and flap. A detailed study of grid convergence is presented to ensure the accuracy of the numerical solutions for the slice-only configuration. Errors in the numerical predictions on different grids were quantitatively determined using the Richardson extrapolation. Aerodynamic force and moment predictions from the codes were compared with wind-tunnel data from the Sandia Mach 8 hypersonic wind tunnel. For the sliced vehicle geometry without the flap, the PNS solutions showed, in general, very good agreement with experimental measurements for body forces and moments. The high accuracy of the numerical solutions for flow over this simple geometry suggest areas where the experimental measurements might be improved.

The PNS code attained only fair agreement with the measurements for the 10-deg flap deflection. For this case, the F3D code agreed very well with the experimental data and it also predicted a small axially separated region ahead of the flap. For flap deflections of 20 and 30 deg, F3D solutions were seriously in error. Although different numerical improvements were investigated for the 20- and 30-deg flap deflections, none were found that improved the agreement with the experimental data. These large flap deflection cases represent a very difficult hypersonics test case for CFD involving shock/boundary-layer/separated flow interaction. Other CFD researchers are encouraged to predict these flowfields and compare them with the experimental data.

Acknowledgments

This work was performed at Sandia National Laboratories, Albuquerque, New Mexico and was supported by the U. S. Department of Energy under Contract DE-AC04-76DP00789. The authors thank Daniel Barnette for his help in running the F3D code and Fred Blottner for his help in executing the grid study. In addition, the help of Roger Tate, Dan Aeschliman, Don Larson, Robert Croll, Ken Harmon, and John Henfling, members of the Aerodynamics Department, is greatly appreciated. All are staff members at Sandia National Laboratories.

References

[1]Oberkampf, W. L., and Aeschliman, D. P., "Joint Computational/Experimental Aerodynamics Research on a Hypersonic Vehicle, Part 1: Experimental Results," *AIAA Journal,* Vol. 30, No. 8, 1992, pp. 2000–2009.

[2]Blottner, F. G., and Larson, E., "Navier-Stokes Code NS3D for Blunt Bodies, Part I: Analysis, Results, and Verification," Sandia National Labs., Rept. SAND88-0504/1, Albuquerque, NM, March 1988.

[3]Blottner, F. G., and Larson, D. E., "Navier-Stokes Code NS3D for Blunt Bodies, Part II: User's Manual," Sandia National Labs., Rept. SAND88-0504/2, Albuquerque, NM, March 1988.

[4]Walker, M. A., "SPRINTRUN: A User Friendly Input Processor for the SPRINT Code," Sandia National Labs., Rept. SAND89-0625, Albuquerque, NM, March 1990.

[5]Stalnaker, J. F., Nicholson, L. A., Hanline, D. S., and McGraw, E. H., "Improvements to the AFWAL Parabolized Navier-Stokes Code Formulation," Air Force Wright Aeronautical Lab., TR-86-3076, Wright-Patterson AFB, Dayton, OH, Sept. 1986.

[6]Schiff, L. B., and Steger, J. L., "Numerical Simulation of Steady Supersonic Viscous Flow," NASA TP 1749, May 1981.

[7]Chaussee, D. S., Patterson, J. L., Kutler, P., Pulliam, T. H., and Steger, J. L., "A Numerical Simulation of Hypersonic Viscous Flows over Arbitrary Geometries at High Angle of Attack," AIAA 19th Aerospace Sciences Conference, AIAA Paper 81-0050, Reno, NV, Jan. 1981.

[8]Rizk, Y. M., Chaussee, D. S., and McRae, D. S., "Computation of Hypersonic Viscous Flow Around Three-Dimensional Bodies at High Angles of Attack," AIAA Fluid and Plasma Dynamics Conference, AIAA Paper 81-1261, Palo Alto, CA, June 1981.

[9]Nicolet, W. E., Shanks, S., and Srinivasan, G., "Flowfield Predictions About Lifting Entry Vehicles," AIAA 20th Aerospace Sciences Conference, AIAA Paper 82-0026, Reno, NV, Jan. 1982.

[10]McWherter, M., Noack, R. W., and Oberkampf, W. L., "Evalu-

ation of Boundary-Layer and Parabolized Navier-Stokes Solutions for Re-Entry Vehicles," *Journal of Spacecraft and Rockets,* Vol. 23, No. 1, 1986, pp. 70–78.

[11]Walker, M. M., and McBride, D. D., "Comparisons of CFD Flow Field Solutions with Experimental Data at Mach 14," *Proceedings of the AIAA Aerodynamic Testing Conference,* AIAA, New York, 1986, pp. 64–77 (AIAA Paper 86-0742).

[12]Bartel, T. J., Homicz, G. F., and Walker, M. A., "Comparisons of Monte-Carlo and PNS Calculations for Rarefied Flow Over Reentry Vehicle Configurations," AIAA 26th Aerospace Sciences Meeting, AIAA Paper 88-0465, Reno, NV, Jan. 1988.

[13]Hudson, M., "Evaluation of PNS-Computed Heating and Hypersonic Shock Tunnel Data on Sharp and Inclined Blunt Cones," AIAA 27th Aerospace Sciences Meeting, AIAA Paper 89-0310, Reno, NV, Jan. 1989.

[14]Steger, J. L., Ying, S. X., and Schiff, L. B., "A Partially Flux-Split Algorithm for Numerical Simulation of Compressible Inviscid and Viscous Flow," *Proceedings of the Workshop on Computational Fluid Dynamics,* Inst. of Nonlinear Sciences, Univ. of California, Davis, CA, 1986.

[15]Ying, S. X., Steger, J. L., Schiff, L. B., and Baganoff, D., "Numerical Simulation of Unsteady, Viscous, High Angle of Attack Flows Using a Partially Flux-Split Algorithm," AIAA Atmospheric Flight Mechanics Conference, AIAA Paper 86-2179, Williamsburg, VA, Aug. 1986.

[16]Srinivasan, G. R., and McCroskey, W. J., "Navier-Stokes Calculations of Hovering Rotor Flowfields," *Journal of Aircraft,* Vol. 25, No. 10, 1988, pp. 865–874.

[17]Blottner, F. G., "Accurate Navier-Stokes Results for the Hypersonic Flow Over a Spherical Nosetip," *Journal of Spacecraft and Rockets,* Vol. 27, No. 2, 1990, pp. 113–122.

[18]Richardson, L. F., and Gaunt, J. A., "The Deferred Approach to the Limit," *Transactions of the Royal Society of London, Series A: Mathematical and Physical Sciences,* Vol. 226, 1927, pp. 229–361.

[19]Walker, M. A., and Oberkampf, W. L., "Joint Computational/Experimental Aerodynamics Research on a Hypersonic Vehicle: Part 2, Computational Results," AIAA 29th Aerospace Sciences Meeting, AIAA Paper 91-0321, Reno, NV, Jan. 1991.